Revue des Composites et des Matériaux Avancés-Journal of Composite and Advanced Materials
Vol. 36, No. 4, August, 2026, pp. 687-700
Journal homepage: http://iieta.org/journals/rcma

Linear and Nonlinear Optical Properties of PMMA–PS/TeO_2 Nanocomposites for Slab Waveguide Applications

Montaser A. Mahdi*, Khalid Al-Ammar, Zaid A. Hasan

Department of Physics, College of Education for Pure Sciences, University of Babylon, Hillah 51001, Iraq

Corresponding Author Email: edu234.mntsr.ahmed@student.uobabylon.edu.iq

https://doi.org/10.18280/rcma.360402

Received: 30 March 2026
Revised: 15 June 2026
Accepted: 25 June 2026
Available online: 31 August 2026

Keywords:
nanocomposites, polymethyl methacrylate, polystyrene, TeO_2, waveguide

ABSTRACT

Polymethyl methacrylate and polystyrene (PMMA-PS) nanocomposites (NCs) doped with TeO_2 nanoparticles (0, 2, 4, and 6 wt%) were prepared using the casting method, and their linear and nonlinear optical (NLO) features were investigated to assess their potential use in slab waveguide devices. As the concentration of TeO_2 increased, the reduction in the optical bandgap energy was consistent with an enhanced absorption coefficient and a redshift in the absorption edge, as corroborated by the attenuation in the optical bandgap energy. Similarly, the refractive index, extinction coefficient, dielectric constant, and optical conductivity increased with higher TeO_2 loading. The NLO properties of the PMMA-PS/TeO_2 NCs were also investigated and exhibited a negative nonlinear refractive (NLR) index, i.e., self-defocusing, as a result of a decrease in refractive index with an increase in incident laser intensity, and a positive NLA coefficient corresponding to two-photon absorption (TPA). The suitability of PMMA-PS/TeO_2 NCs for slab waveguide devices was evaluated using an asymmetric slab waveguide model, which showed an increase in the refractive index of the guiding layer at higher TeO_2 concentrations, thereby increasing the V-number and the number of modes supported by the slab waveguide. Similarly, the refractive indices also indicated the material's compatibility with slab waveguide devices. Field distribution analysis also showed an increase in transverse electric (TE) mode confinement at higher TeO_2 concentrations, thereby supporting the suitability of PMMA-PS/TeO_2 NCs for waveguide devices.

1. INTRODUCTION

Over the previous few years, polymer composite materials have been increasingly utilized in different fields, especially in developing fields like optics and optoelectronics [1]. The fact that polymer composite materials offer several benefits could help explain this, for example, the addition of nanoparticles (NPs), as well as their cheap, flexible, and user-friendly nature. There is a market opportunity for synergistic polymer composites and blends, for example, those containing innovative, synthesized materials [2].

Due to the rapid growth of the fields of optical communications and optoelectronics, there is an increasing environmental contamination issue arising from photonic e-waste driven by growing demand for optical components and devices [3]. Inorganic crystalline waveguides usually require high-energy, energy-intensive manufacturing and etching methods, which may pose environmental challenges during their end-of-life cycle [4]. To improve sustainability and reduce adverse environmental effects, photonic materials based on organic polymers have attracted significant interest as ideal media for green photonics and eco-optical technologies. Low-temperature processable thermoplastic polymers such as PMMA and PS have received considerable interest as ideal materials for optics because of their low density, high transparency, and ease of processing [5]. Thermoplastic polymers may be melted and reprocessed due to their nature, allowing recycling into other optical applications [6, 7].

There are several methods for incorporating polymer materials, and incorporating polymethyl methacrylate (PMMA) and polystyrene (PS) is preferred for research purposes. This thermoplastic polymer is often used to design optical and electronic materials for a variety of purposes, owing to its exceptional combination of properties, including low visibility, low optical absorption, and high mechanical, thermal, and electrical performance. In addition, it is stiff, cheap, easy to produce, and highly transparent in the visible region [8, 9]. Weatherproof, hydrolysis-resistant casings are a preferred application for the aforementioned polymer, especially given its strength as an enclosure material. Although PMMA is a good material, it has a disadvantageous characteristic: a low nonlinear refractive (NLR) index (n_2) [10, 11].

PS is an amorphous thermoplastic polymer that is transparent, flexible, non-opaque, radio-resistant, and

thermally insulating [12, 13]. PS is a valuable additive because it can significantly improve the mechanical and thermal properties of PMMA. Most of the literature on polymethyl methacrylate and polystyrene (PMMA-PS) focuses on its thermal properties when heated [8]. The synergistic combination of these two polymers effectively yields a compound with superior overall structural strength and optimized mechanical performance [14, 15].

Furthermore, the addition of semiconductor nanoparticles to these polymers can greatly improve their nonlinear optical (NLO) properties. Specifically, the semiconductor nanoparticles, namely ZnO, TiO_2, CdS, CdSe, and ZnS, have begun to demonstrate their ability to improve the thermal and structural properties of the compound, in addition to their linear and nonlinear properties [16, 17]. Among these candidates, TeO_2 NPs represent a particularly interesting option. Owing to their unique linear and nonlinear properties, as well as their extreme linear refractive index, it is effective in altering the optical response of other materials [18, 19]. Changes in the linear optical characteristics of TeO_2 NPs implanted in PMMA-PS are anticipated. Matrices and the energy gap (E_g), third-order NLO characteristics such as the PMMA-PS matrix, the NLR index (n_2), and the nonlinear absorption (NLA) coefficient (β).

For these composite materials, the understanding and possible applications depend on an examination of their linear and NLO response. Nonlinear functions describe a material's response to high-power light, such as that from lasers. On the contrary, linear functions such as transmittance, energy gap, and absorption relate to the material's response to low levels of illumination. Complex devices, such as optical limiting devices and switching mechanisms, operate because of the nonlinear characteristics of their operations [20]. For identifying third-order nonlinear characteristics in standard materials, the Z-scan technology is acknowledged as the most sensitive and comprehensive approach [21]. It is possible to measure the signal and amplitude of the NLA coefficient and NLR index (n_2) at the same time, because the method, which entails examining the sample's transmittance along the focused laser beam's propagation axis, is straightforward [22, 23]. Following the discovery that additive concentration can be used to regulate nonlinear features such as saturable absorption (SA) and reverse saturation absorption (RSA), the technique has been used to characterise numerous materials. This enables the method to be applied to the advancement of devices such as optical switches and locators [24, 25].

Thus, this research aims to study the impact of TeO_2 NP concentration on the optical properties of PMMA-PS NPs, especially on refractive index contrast and, consequently, on confinement, propagation, and modal characteristics of TE modes of asymmetric slab waveguides designed as eco-friendly optical components.

2. EXPERIMENTAL WORK

PMMA-PS/TeO_2 nanocomposite films that were studied in this experiment were prepared by using the solution casting process. The exact amounts of the components used in the process (0.8 g PS + 0.2 g PMMA), the exact concentration of TeO_2 nanoparticles (2, 4, 6 wt%) as well as the exact parameters of dispersion process, namely, the duration of magnetic stirring process (1 h) and probe sonication (2 h) were kept exactly as optimized in our prior study [26]. The TeO_2 NPs were purchased from NanoChemazone Inc. (Canada) with a nominal average particle size of less than 100 nm and were used as received without further surface modification. TeO_2 NPs were added to the polymer solution in exact nominal weight percentages of (2, 4, 6 wt%) while the solution was being prepared. A magnetic stirrer and an ultrasonic probe were used alternately to stir the solution, ensuring that the nanoparticles are uniformly distributed and that no agglomeration occurs (Note on Environmental, Health, and Safety (EHS) Considerations).

Table 1. Experimentally measured parameters of PMMA-PS/TeO_2 NCs

TeO_2 (wt%)	Thickness (μm)
0	170 ± 20
2	176 ± 20
4	179 ± 20
6	182 ± 20

Note: PMMA-PS = polymethyl methacrylate and polystyrene, NCs = nanocomposites.

In terms of EHS, the processing and handling of the PMMA-PS/TeO_2 nanocomposite material involved the implementation of rigorous safety standards. Chloroform was chosen as the solvent in light of its thermodynamic interaction with PMMA and PS, which is capable of preventing phase segregation and ensuring the optical transparency needed for waveguide operation. The VOC emissions were further controlled by performing all dissolutions and casting processes within a properly certified, high-efficiency chemical fume hood that was fitted with carbon filters for solvent vapor recovery. Lastly, upon activation of the prepared photonic film, the heavy TeO_2 nanoparticles were firmly encased in the complex three-dimensional polymeric structure. Therefore, the robust encapsulation was highly expected to minimize the likelihood of nanoparticle release into the surrounding environment during standard operational handling; however, its ultimate stability under long-term severe mechanical abrasion remains to be fully evaluated. Finally, all unused raw materials and film scraps after characterization were carefully recycled through the hazardous waste disposal process that either incinerates them or separates polymers from solvents. The success of elemental composition and loading of these nanocomposites (NCs) under the same conditions has already been proven and verified in previous research by our team using the Energy Dispersive X-ray (EDX) spectroscopy method [26]. To ensure the surface is clean and suitable for membrane production, substrates, such as Petri dishes, were cleaned using distilled water and ethanol prior to the casting procedure. Direct casting was used to produce composite thin nanofilms of PMMA-PS/TeO_2 on these pristine substrates. Next, they were left to dry for three days at room temperature. This step was extremely important in ensuring that the solvent was completely evaporated and that solid membranes were obtained. The PMMA-PS/TeO_2 NCs were prepared for various measurements and tests by removing them from Petri plates after drying was complete. The actual thickness of the prepared films was measured using a digital micrometer, and the average thickness values (mean ± standard deviation (SD)) for the samples are detailed in Table 1. A UV-160 visible Shimadzu spectrophotometer was used, operating in the wavelength range from 220 nm to 1200 nm with a scanning speed of 1500 nm/min. The λ = 405 nm CW diode laser used in the Z-scan experiments had a maximum power of 50 mW,

an AC voltage of 220-240 volts, a frequency of 50-60 Hz, and a current of 250 mA. The beam was focused using a 10 cm focal-length lens, with a 1.5 mm diameter and a divergence of 1.5 mrad. The Rayleigh length (Z0) is 0.92 cm, and the laser beam waist radius ω_0 at the focus is 0.015 mm. The geometric parameters used in the Z-scan experiments are summarized in Table 2.

Table 2. Geometric parameters for the Z-scan experimental setup

Symbol	Values
ω_0	0.015 mm
Z_0	0.92 cm
S	0.2
P_{max}	50 mW

Note: ω_0 is the beam radius, Z_0 is the Rayleigh length, S is the linear transmittance of the aperture, and P_{max} is the maximum laser power.

In order to guarantee reliable and reproducible results, all experiments for linear and NLO property measurements have been carried out two times (n = 2) under equal experimental conditions. High precision of the data obtained in the experiments and parameters of the curve fit was achieved since the SDs and curve fitting errors calculated did not exceed the threshold of accuracy within ±2.5% (maximum error of the instrument), which is related to the optical power meter calibration.

3. RESULTS AND DISCUSSION

3.1 Optical microscopy

Figure 1 shows optical microscopy (OM) images of pure PMMA-PS polymer blend and PMMA-PS/TeO_2 NCs prepared with different concentrations of TeO_2 NPs, at 10× magnification. After TeO_2 NPs were added, a network was formed during the first phase of the (PMMA-PS) mixture as the TeO_2 content increased. Carriers will move through the channels of this network, changing the material's characteristics [27, 28].

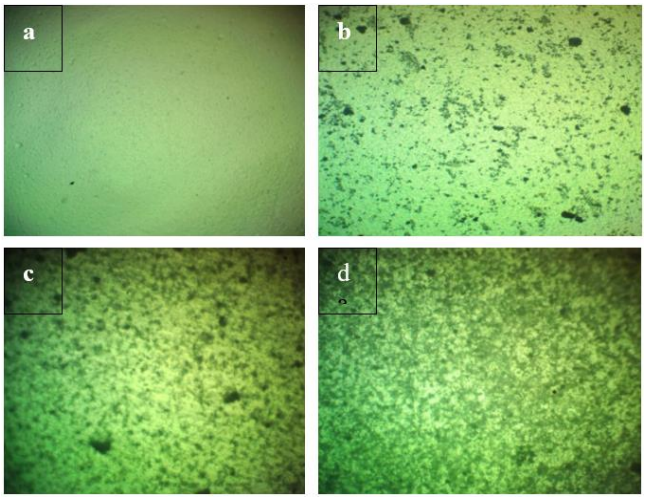

Figure 1. Microscope images (×10) for PMMA-PS/TeO_2 (a) blend, (b) 2 wt% TeO_2, (c) 4 wt% TeO_2, and (d) 6 wt% TeO_2
Note: PMMA-PS = polymethyl methacrylate and polystyrene.

In comparison with pure polymer blend films, optical micrographs showed some morphological variations in the surface as the amount of TeO_2 increased in PMMA-PS/TeO_2 NC films. The presence of nanoparticles was responsible for such morphological variations, while no significant agglomeration was observed for this material even at the highest concentration at the 10× OM magnification, ensuring that the films were transparent enough for waveguiding and optical applications. On the other hand, from the optical micrograph images, a macroscopically homogeneous dispersion of the nanoparticles could be seen on the surface of the film for all samples (Figure 1(a)-(c)), especially for the samples with higher concentrations, as shown in Figure 1(d). Nevertheless, since OM at the 10× magnification still suffers from the resolution limitation in resolving sub-micron agglomerates or even individual nanoparticles, an extensive verification of the high-resolution dispersion of the nanoparticles, internal morphology, and particle size distribution of the very same batch of samples was performed using Field Emission Scanning Electron Microscopy (FESEM) in a separate study [26]. The FESEM images confirmed that TeO_2 nanoparticles could form extremely homogeneous dispersion not only in the sub-micron region but also in the nanometer range in polymer blends, suggesting that the ultrasonically assisted approach applied herein works well [29].

3.2 Optical properties

Figure 2 shows the absorbance of PMMA-PS/TeO_2 NCs as a function of incoming light wavelength. PS-PMMA films show no absorbance between 280 and 1080 nm, which is a broad wavelength range. For high photon energy, the NCs exhibit high absorption. At all TeO_2 concentrations, adding TeO_2 to the PMMA-PS mixture causes the absorption edge to shift toward longer wavelengths and raises the short-wavelength absorption intensity region. The rise in absorbance with increasing filler content makes sense since TeO_2 atoms absorb incoming light [30, 31]. The shift of the absorption edge towards higher wavelengths decreases the optical energy gap, indicating a change in the electronic structure's energy levels [32]. Furthermore, the absence of an absorption band in the visible spectrum of these samples indicates that they are transparent in this spectrum [33]. The absorbance of PMMA-PS increased by around 28% when the TeO_2 concentration reached 6%. The formula for absorbance (A) is given below [34].

$$A = log_{10}\frac{I_0}{I_T} \quad (1)$$

where, I_0 is the incident light intensity, and I_T is the transmitted light intensity through a sample.

Figure 3 shows the transmittance spectra for films of PMMA-PS/TeO_2 NCs with different concentrations of TeO_2 NPs. Transmittance increased rapidly with wavelength and decreased with TeO_2 NPs loading [35]. Light from the PMMA-PS film is absorbed and scattered by TeO_2 NP. This is attributed to the way the electrons in the outer shells of TeO_2 NPs capture the energy from the incoming photons and transition to a higher energy level. As the electrons occupy the higher energy levels in the energy range, the level of absorption of the photons increases, and more of the photons are blocked [36, 37]. Transmittance (T) is computed as in Eq. (2) [38].

$$T = \frac{I_T}{I_0} \quad (2)$$

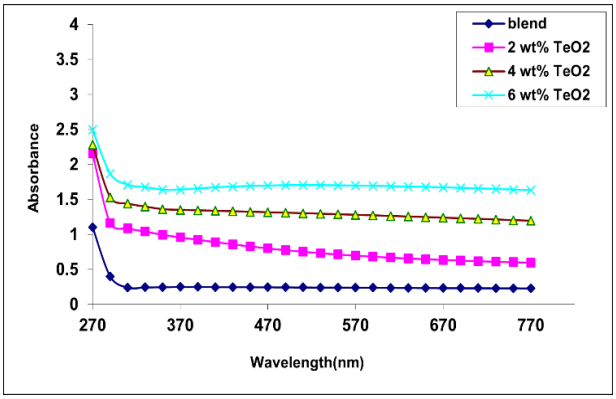

Figure 2. Ultraviolet-visible (UV-Vis) absorbance spectra of PMMA-PS/TeO_2 NCs as a function of wavelength
Note: PMMA-PS = polymethyl methacrylate and polystyrene.

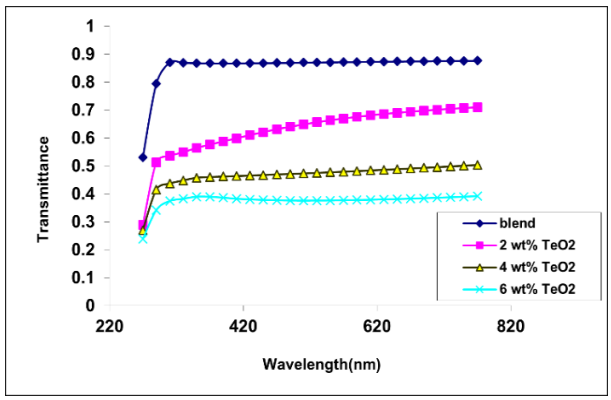

Figure 3. Transmittance variation with wavelength for PMMA-PS/TeO_2 NCs
Note: PMMA-PS = polymethyl methacrylate and polystyrene, NCs = nanocomposites.

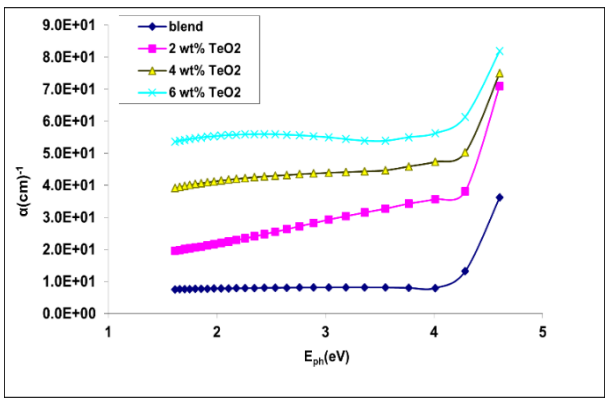

Figure 4. Absorbance coefficient (α) variation with E_{ph} for PMMA-PS/TeO_2 NCs
Note: PMMA-PS = polymethyl methacrylate and polystyrene, NCs = nanocomposites.

Figure 4 shows how absorption coefficients change with wavelength, with absorption being at its lowest when the energy is low. This indicates that an electron cannot be transferred from the valence energy band to the conduction energy band ($h\upsilon < E_g$) using the photon's energy. However, when the photon energy (ph_E) increases above 3.4 eV, it leads to more frequent electronic transitions, causing electrons to move from the valence energy band to the conduction energy band. At this point, the photon energy is sufficient to allow the electron to cross the forbidden energy gap ($h\upsilon > E_g$). One possible indicator of the type of electron transition is a high absorption coefficient ($\alpha > 10^4$ cm^{-1}). Phonons conserve electron momentum, while electrons move indirectly when the absorption coefficient is low ($\alpha < 10^4$ cm^{-1}).

Therefore, at all concentrations, the (PMMA-PS/TeO_2) NCs showed an absorption coefficient (α) of less than 104 cm^{-1}. As the concentration of TeO_2 NPs in NCs rises, so does the absorption coefficient. This can be explained by an increase in charge carriers, which raises both the absorption and absorption coefficient of the NCs [39, 40]. The absorption coefficient (α) of the materials used nowadays is determined by Eq. (3).

$$\alpha = 2.3\,\frac{A}{t} \quad (3)$$

Figures 5 and 6 illustrate the allowed and forbidden indirect E_g transitions for PMMA-PS/TeO_2 NCs. The optical E_g for the allowed and forbidden indirect transitions is shown at $r = 2$ and $r = 3$, respectively. A decrease in the optical gap values is observed with increasing TeO_2 NPs concentration, leading to the transfer of electrons from the valence energy band to lower energy levels in the conduction energy band. In this case, the transition occurs via a multi-step process [41, 42].

The relationship is used to calculate the indirect transition.

$$\alpha h\upsilon = B\left(h\upsilon - E_g^{opt}\right)^r \quad (4)$$

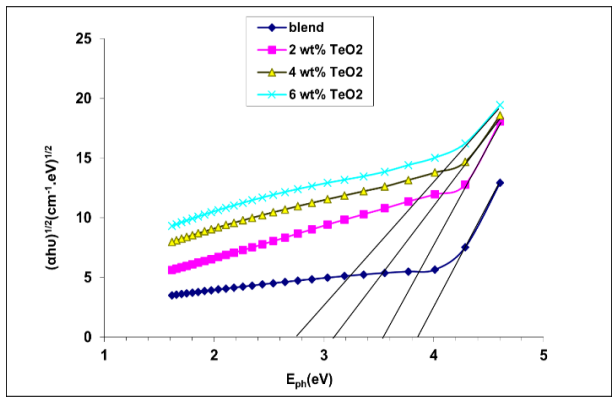

Figure 5. Differences of $(\alpha h\upsilon)^{1/2}$ for (PMMA-PS/TeO_2) with E_{ph}
Note: PMMA-PS = polymethyl methacrylate and polystyrene.

Figure 7 shows the extinction coefficient (k) of PMMA-PS/TeO_2 NCs as a function of photon wavelength. k is related to the absorption loss. Alternatively, it is the amount of loss in light intensity due to scattering and absorption as an electromagnetic wave travels through a material. As photon energy increases, k falls, suggesting a greater proportion of light is lost as a result of absorbance and scattering [43]. Moreover, the loss ratio rises in direct proportion to photon energy. The TeO_2 NPs absorbed the incoming photons [44, 45]. At low concentrations, the value of k is found to be smaller due to reduced photon absorption and photon scattering in the blend matrix. Enhancing the doping ratio of NPs within the blend matrix leads to an enhancement in the absorption coefficient, and consequently, a higher k [46, 47].

$$k = \frac{\alpha\lambda}{4\pi} \quad (5)$$

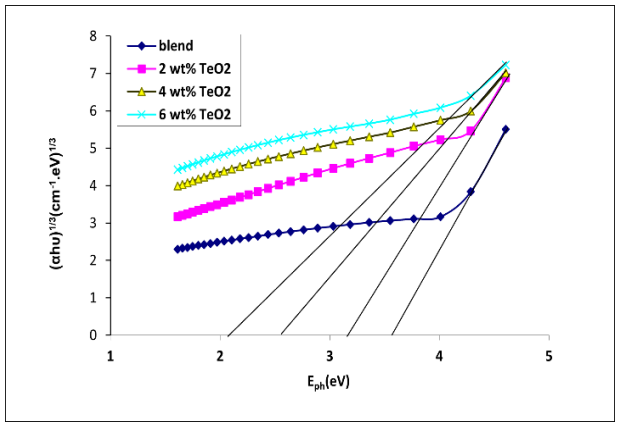

Figure 6. Differences of $(\alpha h\upsilon)^{1/3}$ for (PMMA-PS/TeO_2) NCs with E_{ph}

Note: PMMA-PS = polymethyl methacrylate and polystyrene, NCs = nanocomposites.

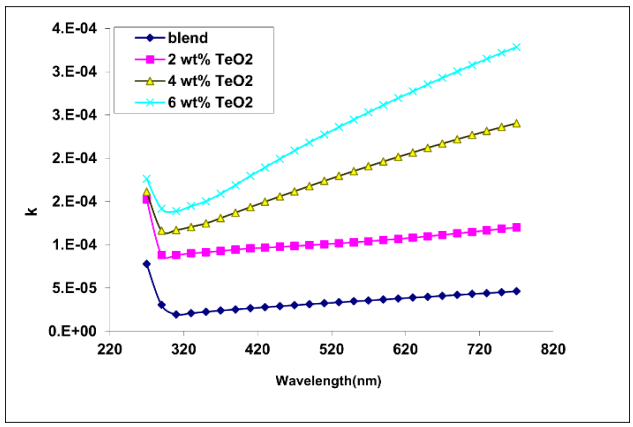

Figure 7. Differences in extinction coefficient (k) for (PMMA-PS/TeO_2) with wavelength

Note: PMMA-PS = polymethyl methacrylate and polystyrene.

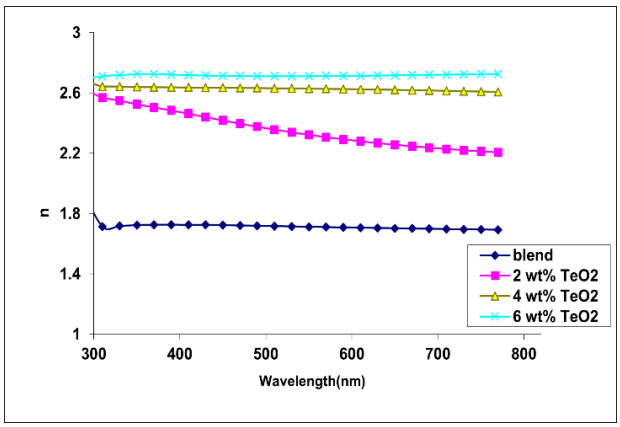

Figure 8. Refractive index variation with wavelength for PMMA-PS/TeO_2 NCs

Note: PMMA-PS = polymethyl methacrylate and polystyrene, NCs = nanocomposites.

The differences in the refractive index with wavelength for PMMA-PS/TeO_2 are seen in Figure 8. As the wavelength of PMMA-PS/TeO_2 NCs increases, their refractive index falls. Reflectance mostly determines the refractive index. Refractive index and reflectance increase with increasing TeO_2 concentration, suggesting an increase in density [48, 49]. Due to low transmittance in the ultraviolet (UV) region, the refractive index is higher there, whereas high transmittance causes it to be lower in the visible and near-infrared regions [50]. The refractive index (n) is calculated from Eq. (6).

$$n = \frac{R+1}{R-1} + \left[\frac{4R}{(R-1)^2} - K_0^2\right]^{0.5} \quad (6)$$

Figure 9 shows the response of the real component of the dielectric constant, and Figure 10 shows the response of the imaginary component of the PMMA-PS/TeO_2 NCs to changes in wavelength. The results showed that increasing the TeO_2 NPs concentration in the PMMA-PS polymer blend enhances the sample's electrical polarization, thereby enhancing both the real and imaginary components of the blend's dielectric constant. Wavelength affects the dielectric constant, and the refractive index influences the real component of the dielectric constant [51]. The response of the imaginary component of the dielectric constant is also affected by enhancing the absorption coefficient [52]. Interestingly enough, there is a rather high profile of the effective refractive index of these engineered films. As noted above, with advanced dielectric and effective medium approaches, this extraordinary optical property can exceed the regular bulk limitations of the individual constituents [53]. Such behavior can be explained by the enhanced interfacial electronic polarizability and electric field enhancement that occur at the interfaces between TeO_2 nanoparticles and their surrounding PMMA-PS polymer matrices [53, 54]. Indeed, this remarkable electrostatic and dipole-dipole interaction within the sub-micron dimensions leads to the pronounced optical field enhancement. In combination with the changes in the packing density of the host polymer and free volume of its polymer chain [55], this creates a strong physical explanation for the high-performance index modulation up to saturation around 4–6 wt%. The real and imaginary parts of the dielectric constant can be derived as follows [56]:

$$\varepsilon_r = n^2 - k_0^2 \quad (7)$$

$$\varepsilon_i = 2nk \quad (8)$$

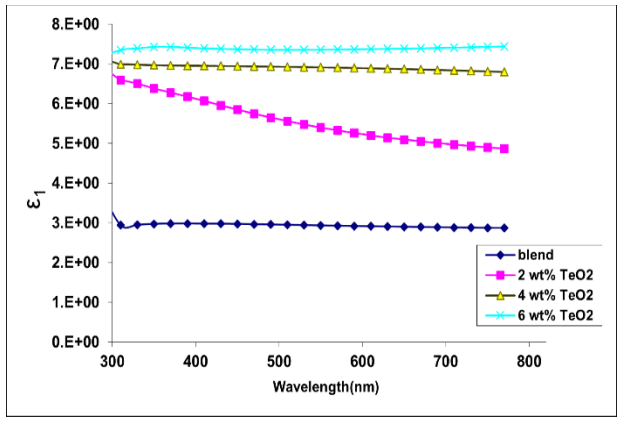

Figure 9. The real dielectric constant for PMMA-PS/TeO_2 NCs with wavelength

Note: PMMA-PS = polymethyl methacrylate and polystyrene, NCs = nanocomposites.

Figure 11 illustrates the connection between ph_E and optical conductivity. The behavior of doped and pure samples differs.

The optical conductivity rises at low photon energies and subsequently falls at higher ph_E; as optical conductivity depends on the absorption coefficient, this behavior is similar to that of the absorption coefficient [57]. Moreover, the addition of TeO_2 NPs enhanced optical conductivity; this result is explained by the formation of localized levels in the energy gap, which increased with the concentration of TeO_2 NPs. The density of localized states in the band structure rises with the number of NPs [27].

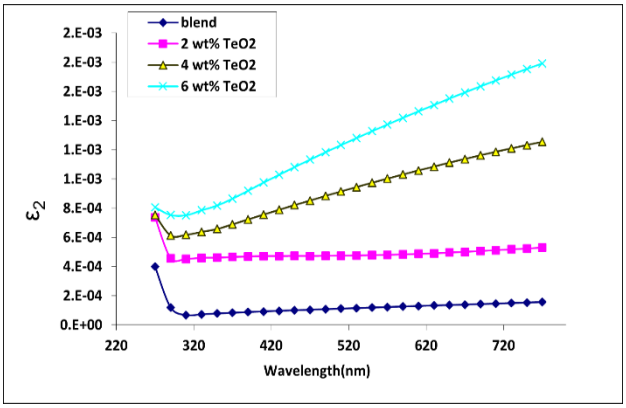

Figure 10. The imaginary part of the dielectric constant for PMMA-PS/TeO_2 NCs with wavelength
Note: PMMA-PS = polymethyl methacrylate and polystyrene, NCs = nanocomposites.

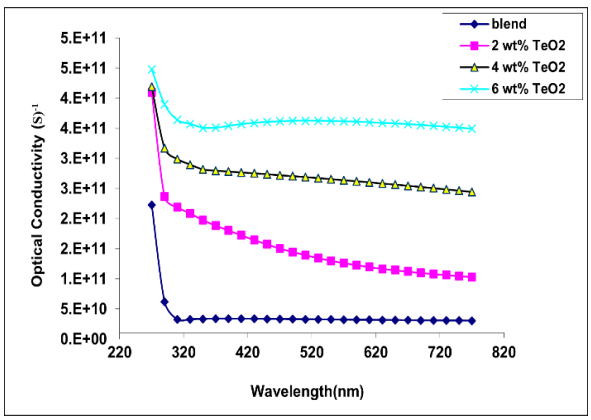

Figure 11. Variation of optical conductivity for PMMA-PS/TeO_2 NCs with wavelength
Note: PMMA-PS = polymethyl methacrylate and polystyrene, NCs = nanocomposites.

3.3 Nonlinear optical characteristics

The NLR index (n_2) of the PS-PMMA/TeO_2 NCs with varying TeO_2 loadings (2, 4, and 6 wt%) was determined using the closed-aperture (CA) Z-scan technique. Figure 12 demonstrates how the normalized transmittance of the Z-scan measurements changes with distance. This chart shows that the nonlinear effect zone goes from -3 mm to 3 mm. The peak and valley transmittance curve derived from the CA Z-scan data demonstrates that the NLRe signal is negative ($n_2 < 0$), resulting in self- defocusing in these samples. Under CW laser irradiation with a wavelength of λ = 405 nm, the NLR index (n_2) is dominated by photothermal localized effects rather than being dependent on the electronic structure of the material. As the laser beam continues to be absorbed within the polymer nanocomposite layer, a temperature difference develops throughout the polymer matrix, following the Gaussian profile of the laser beam intensity. Since polymers such as PMMA and PS have a negative thermo-optic effect ($dn/dT < 0$), the refractive index reduces in regions with high temperatures (the center of the laser beam). Therefore, the index modification causes thermal lensing with negative values (self-defocusing) of the refractive index ($n_2 < 0$) [58]. "In addition, it can be seen that the normalized transmittance reduces as the weight of the nanoparticles increases. The cause behind this trend is that with an increase in the weight of TeO_2 nanoparticles, the optical absorbance of the samples increases. As a result, a larger temperature gradient develops and the thermal lens efficiency of the polymer medium increases. As a result of these effects, a larger change in the value of nonlinear phase change (ΔΦ°) takes place. In turn, this leads to a larger value of the effective NLR index (n_2). Thus, n_2 is dependent on the weight of TeO_2 nanoparticles in the NCs. This is consistent with previous work [17]. The different transmittance values of the CA Z-scan were used to calculate the nonlinear phase shift ΔΦ° and the NLR index (n_2).

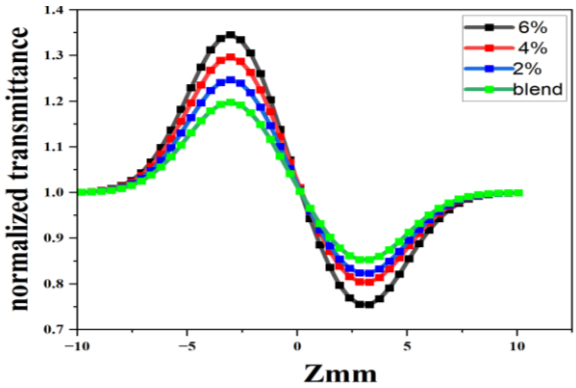

Figure 12. CA Z-scan data for (blend, 2, 4, and 6 wt%) of (PMMA-PS/TeO_2) NCs
Note: Closed-aperture (CA), PMMA-PS = polymethyl methacrylate and polystyrene, NCs = nanocomposites.

ΔΦ° can be computed using [59]:

$$\Delta\Phi^\circ = \frac{\Delta T_{p-v}}{0.466(1-s)^{0.25}} \quad (9)$$

where, ΔT_{p-v} is defined as the shift in transmittance between the peak and the valley in a Z-scan with a closed aperture.

$$\Delta T_{p-v} = T_P - T_v$$

where, T_p and T_v represent the peak and valley's normalised transmittance, as shown in Figure 4. Selecting the size of the aperture can help to produce better results. The parameter S was set to 0.2, which falls within the range of 0.1 to 0.5 commonly used in previous experimental studies [60].

Consequently, the NLR index (n_2) may be computed using the values of ΔΦ° [61]:

$$n_2 = \frac{\lambda\Delta\Phi^\circ}{2\pi I_0 L_{eff}} \quad (10)$$

where, I_0 is the peak on-axis laser intensity at the focus computed by:

$$I_0 = \frac{2P_{in}}{\pi\omega_0^2} \quad (11)$$

where, λ is the laser source's wavelength, and L_{eff} is the sample's effective length, which is calculated as:

$$L_{eff}=\frac{1-e^{-\alpha d}}{\alpha} \quad (12)$$

Table 3 lists the PMMA-PS/TeO_2 NCs' values for ΔΦ°, L_{eff}, and n_2.

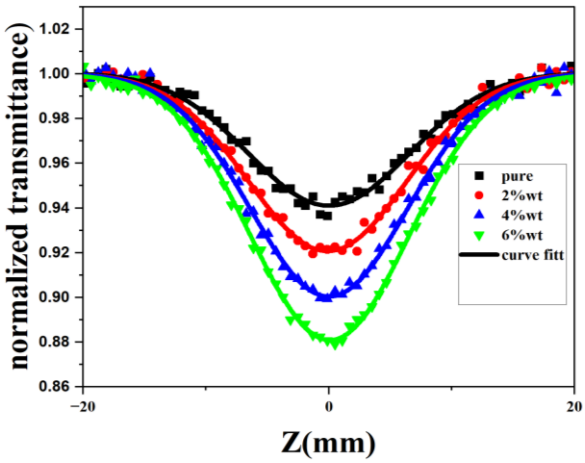

Figure 13. Open-Aperture (OA) Z-scan data for (blend, 2, 4 and 6 wt%) of PMMA-PS/TeO_2 NCs
Note: PMMA-PS = polymethyl methacrylate and polystyrene, NCs = nanocomposites.

Figure 13 shows the normalized transmittance curves as a function of the sample position on the optical axis (Z), where the open-aperture (OA) Z-scan technique was used to study the NLO absorption of PMMA-PS/TeO_2 NCs with weight percentages of (0, 2, 4, and 6 wt%) of TeO_2 under a Gaussian laser excitation. All samples show a symmetrical dip at the focal position (Z = 0), and the depth of this dip increases with increasing TeO_2 doping. This behavior is evidence of positive NLO, which is attributed to two-photon absorption (TPA) or RSA [62]. Since the laser intensity is at its maximum at the focal point, this increases the probability of multi-photon electronic transitions. Increasing the incorporation of TeO_2 NPS leads to the formation of local energy levels within the polymer's energy gap and an increase in the density of effective electronic states, thus increasing the probability of TPA [63, 64]. The inspection data were analyzed using the Sheik-Bahae model of nonlinear absorption (β), where the normalized transmittance for the open aperture is given by the approximate relationship [2].

$$T(Z) = 1-\frac{\beta I_0 L_{eff}}{2\sqrt{2}-(1+\frac{z^2}{z_0^2})} \quad (13)$$

where,

β represents nonlinear absorption, I_0 is the laser beam's, L_{eff} is the sample's effective length, and Z_0 is the Rayleigh length. Table 3 lists the values of β and other nonlinear parameters.

Table 3. The obtained values of NLR (n_2) index phase shift (Δϕ), NLA coefficient (β), NLR coefficient (n_2), pure (PMMA/PS) and PMMA-PS/TeO_2 NCs under CW laser excitation at λ = 405 nm

TeO_2 (wt%)	I_0 (MW/m²)	Absorbance	α (cm^{-1})	L_{eff} ($\times 10^{-4}$ m)	ΔT_{p-v}	ΔΦ° (rad)	$n_2 \times 10^{-12}$ (m^2/W)	$\beta \times 10^{-10}$ (m/W)
0	15.513	0.055872	4.289	9.979	0.34	0.7714	-3.21	3.8992
2	15.513	0.213781	16.411	9.918	0.41	0.9303	-3.899	4.5436
4	15.513	0.456592	35.051	9.827	0.49	1.1118	-4.703	5.2331
6	15.513	0.604837	46.431	9.771	0.59	1.3387	-5.695	6.0052

4. OPTICAL WAVEGUIDE ANALYSIS

4.1 Waveguide structure and parameters

Indeed, it should be noted that while the NCs were formed using the solution casting technique and their thickness was about 170–182 μm, a much thinner core film thickness of 1 μm was employed in the slab waveguide simulation. In integrated micro-photonic devices, the use of a thick core of hundreds of micrometers results in very high modal density (multimodal transport) with very strong scattering loss, and it becomes difficult to perform single- to few-mode light transport. Consequently, the core thickness of 1 μm was considered in order to estimate the light guiding capacity of the composite material for single- to few-mode transport in photonic applications. Although such a thin core can be accurately deposited using the spin-coating process, utilizing the optical constants (n and α) obtained from the thicker experimental films (170–182 μm) for this 1 μm simulation serves as a theoretical approximation, assuming a thickness-independent constant as a limitation of the current model.

The fabricated PMMA–PS/TeO_2 nanocomposite films were modeled as an asymmetric slab waveguide with three layers, as schematically illustrated in Figure 14: a substrate, a nanocomposite film (core), and air (cover). The refractive indices of the layers are represented by the symbols n_c, n_f, and n_s. The substrate and cover refractive indices were assumed to be constants, while the core layer's refractive index was determined through ultraviolet-visible (UV-Vis) analysis. The analysis also accounted for the operating wavelength and the thickness of the core layer.

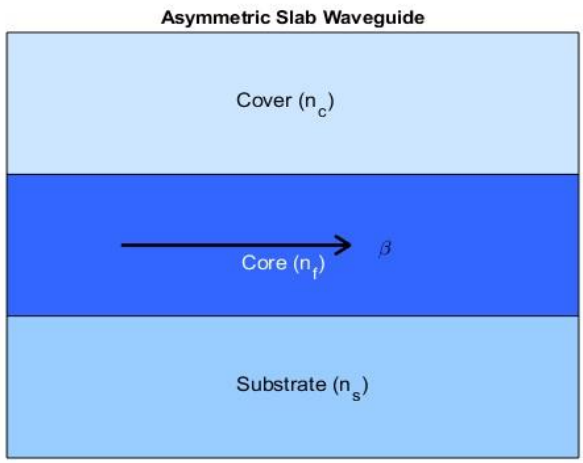

Figure 14. Transverse section of rectangular slab waveguide

The three layers that make up the planar waveguide have the following refractive indices.

Substrate refractive index (n_s): The glass substrate has a well-established refractive index of n_s = 1.52 at λ = 633 nm [65].

Upper cladding refractive index (n_c): The upper cladding layer consists of ambient air, which maintains a refractive index of n_3 = 1.000 under standard temperature and pressure conditions.

Core refractive index (n_f): The refractive index of the polymer nanocomposite core is measured experimentally for each TeO_2 concentration using UV-Vis spectroscopy, and the values are extrapolated to a 633 nm thickness of the core of 1 µm. A constant film thickness of 1 µm was taken in the calculations of the slab waveguide model. This thickness value was chosen because it is considered to be a common thickness of the polymers used in polymer optical waveguides.

4.2 Mathematical formulation of the slab waveguide

The normalized frequency, also known as the V-number, is a dimensionless number that specifies the efficiency with which a particular waveguide type confines and carries a specific type of electromagnetic signal. The normalized frequency can be defined as follows [66]:

$$V=kh\sqrt{n_f^2-n_s^2} \tag{14}$$

where, $k = \frac{2\pi}{\lambda}$, h is the core thickness, λ is the operating wavelength, n_f is the core refractive index, and n_s is the substrate refractive index.

For an asymmetric planar waveguide (where $n_c \neq n_s$), the number of guided transverse electric (TE) modes can be estimated using the approximate formula:

$$M_{total}=\frac{2V}{\pi} \tag{15}$$

An asymmetry factor a, which is dependent on the mode's polarisation, represents the waveguide's asymmetry. Regarding TE modes, we have [67]:

$$a_E = \frac{n_2^2-n_3^2}{n_1^2-n_2^2} \tag{16}$$

The guided modes are obtained by solving the dispersion equation of the asymmetric slab waveguide [68]:

$$hd-tan^{-1}\left(\frac{p}{h}\right)-tan^{-1}\left(\frac{q}{h}\right)=m\pi \tag{17}$$

where, the parameters h, p, and q are defined as:

$$h = k_0\sqrt{n_f^2-n_{eff}^2}$$
$$p = k_0\sqrt{n_{eff}^2-n_s^2}$$
$$q = k_0\sqrt{n_{eff}^2-n_c^2}$$

The above equation is solved numerically to determine the effective refractive index (n_{eff}) for each guided mode, where the condition $n_s < n_{eff} < n_f$ must be satisfied.

The propagation constant β_m for mode m represents the phase change per unit length along the propagation direction (z-axis). It is a fundamental parameter in waveguide theory and is defined as [69]:

$$B = \frac{2\pi}{\lambda}n_{eff} \tag{18}$$

The curves of the normalized propagation constant (b) as a function of the normalized frequency or V-number (b-V) were plotted using MATLAB with the calculated values of b for different values of V-number. Each curve represents a specific guided mode, and the number of modes increases with increasing normalized frequency. For this purpose, the normalized form of the dispersion equation was considered, which can be expressed as [66, 70]:

$$V\sqrt{1-b} = tan^{-1}\left(\sqrt{\frac{aE+b}{1-b}}\right)+tan^{-1}\left(\sqrt{\frac{b}{1-b}}\right)+m\pi \tag{19}$$

The analytical solutions of the Helmholtz equation were used to simulate the TE field distribution, and MATLAB was used to compute and plot the guided TE mode profiles [71].

$$E_y(x) = \begin{cases} sin\phi e^{px}, & x < 0\ (substrate) \\ sin\ (hx_+\phi), & 0 \le x \le d\ (core) \\ sin\ (hx_+\phi)e^{-q(x-d)}, & x > d\ (in\ air) \end{cases} \tag{20}$$

4.3 Numerical solution using MATLAB

The dispersion equation for the asymmetric slab waveguide has been solved numerically using the MATLAB programming language. The analytical solution of the transcendental equation is not possible; hence, a numerical solution has been applied. n_{eff} of the asymmetric slab waveguide has been calculated by finding the solution of the dispersion equation within the physical limits defined by the inequality:

$$n_s < n_{eff} < n_f$$

The dispersion equation for the supported modes of the asymmetric slab waveguide has been solved using the first set of trial data. The equation's solution matches the asymmetric slab waveguide's supported TE modes.

Once the refractive index has been obtained, the propagation constant β, normalized propagation constant b, and phase velocity v can be calculated using the corresponding equations defined in the previous section.

The numerical solution has been applied for various concentrations of TeO_2 to study its effect on the performance of the asymmetric slab waveguide.

4.4 Analysis results and discussions of waveguide analysis

Table 4 shows the number of guided modes, which increases with the concentration of TeO_2 NPs. This is due to the enhancement in the normalized frequency, V-number, which depends directly on the refractive index difference between the core and the substrate. An increase in the refractive index of the core means that more solutions of the equation are possible, hence the excitation of higher modes.

It was observed that the number of guided modes remains

constant at higher concentrations, specifically 4% and 6%, indicating a saturation effect. This happens when the normalized frequency becomes sufficiently large, and any increase in V does not show a significant contribution to the formation of new guided modes.

Table 4. Modal analysis of the asymmetric slab waveguide with various TeO_2 wt%

TeO_2 (wt%)	n_f	V-Number	a_E	N of Modes
PURE	1.7050	7.6670	2.1964	3
2	2.2660	16.6815	0.464	6
4	2.6224	21.2115	0.2870	7
6	2.7166	22.3491	0.2585	7

The asymmetry factor reduces as the concentration increases. This shows that the waveguide structure becomes more symmetric. This results in better confinement and more stable propagation characteristics.

Table 5. Optical parameters of transverse electric (TE) modes for 0 wt% TeO_2-doped slab waveguide

TeO_2 (wt%)	Mode	n_{eff}	β ($\times 10^7$ m^{-1})	b
0	TE_0	1.6847	1.6722	0.8847
	TE_1	1.6238	1.6118	0.5472
	TE_2	1.5289	1.5176	0.0455

Table 6. Optical parameters of transverse electric (TE) modes for 2 wt% TeO_2-doped slab waveguide

TeO_2 (wt%)	Mode	n_{eff}	β ($\times 10^7$ m^{-1})	b
2	TE_0	2.2480	2.2314	0.9712
	TE_1	2.1933	2.1770	0.8851
	TE_2	2.0996	2.0841	0.7428
	TE_3	1.9630	1.9484	0.5463
	TE_4	1.7772	1.7641	0.3003
	TE_5	1.5422	1.5308	0.0241

Table 7. Optical parameters of transverse electric (TE) modes for 4 wt% TeO_2-doped slab waveguide

TeO_2 (wt%)	Mode	n_{eff}	β ($\times 10^7$ m^{-1})	b
4	TE_0	2.6062	2.587	0.9815
	TE_1	2.5573	2.5383	0.9261
	TE_2	2.4738	2.4555	0.8342
	TE_3	2.3528	2.3354	0.7063
	TE_4	2.1893	2.1732	0.5437
	TE_5	1.9755	1.9609	0.3487
	TE_6	1.7003	1.6877	0.1271

Table 8. Optical parameters of transverse electric (TE) modes for 6 wt% TeO_2-doped slab waveguide

TeO_2 (wt%)	Mode	n_{eff}	β ($\times 10^7$ m^{-1})	b
6	TE_0	2.7009	2.6809	0.9832
	TE_1	2.6533	2.6337	0.9329
	TE_2	2.5722	2.5532	0.8494
	TE_3	2.4550	2.4369	0.7331
	TE_4	2.2970	2.2800	0.5851
	TE_5	2.0911	2.0756	0.406
	TE_6	1.8260	1.8125	0.2020

Also, it should be noted that the relationship between the estimates for the waveguide capacity boundaries based on the equation and its numerical output should be explained. Though the expression considered by the developed mathematical model is the starting point used for defining the total capacity for the waveguide (taking into account both the TE modes and transverse magnetic (TM) modes), this research work focuses exclusively on the calculation of TE modes. Therefore, the designed MATLAB solution was made to calculate and obtain the exact values for the effective refractive index (n_{eff}) roots only for TE modes. A tight convergence tolerance for computation of 10^{-6} to ensure numerical stability and accuracy in finding the roots. Tables 5-8 show the values of the effective refractive index (n_{eff}) for the TE modes exhibit behavior consistent with the asymmetric dielectric slab waveguide theory, as all values remain within the guiding range $n_f > n_{eff} > n_s$, which confirms the fulfillment of the guidance condition within the core layer. It is also noted that n_{eff} decreases by increasing the order of the mode from TE_0 to TE_2, because the higher modes have a greater field penetration in the air and substrate and are less confined inside the core layer. In addition, the n_{eff} values are clearly rising with an increase in the concentration of TeO_2 NPs. This is due to the increase in the refractive index nf of the film, thereby increasing the refractive index and strengthening the wave confinement. Also, increasing the V-number with distortion leads to the transition of modes away from the cutoff boundaries and improves their wave stability. This effect is especially pronounced in the TE_2 mode, which is near the cutoff threshold in the pure sample and then becomes well-guided in the nanoparticle doping.

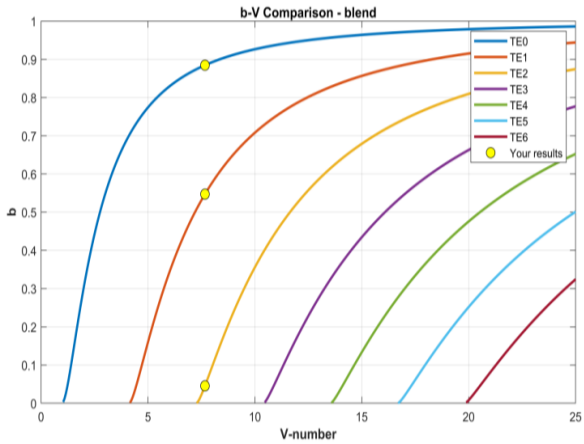

Figure 15. Transverse electric (TE) mode b-V diagram directed by a linear exponential graded index of pure

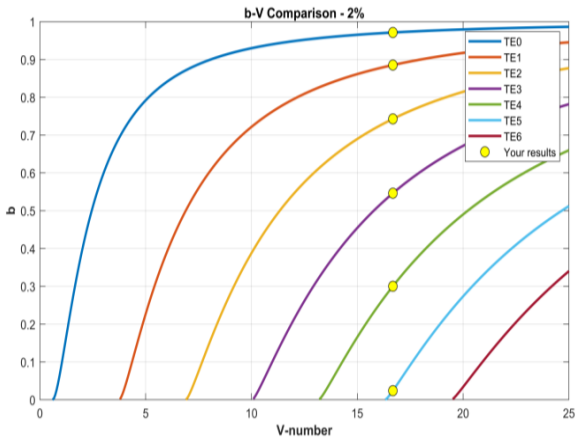

Figure 16. Transverse electric (TE) mode b-V diagram directed by a linear exponential graded index of 2 wt% TeO_2 nanoparticles (NPs)

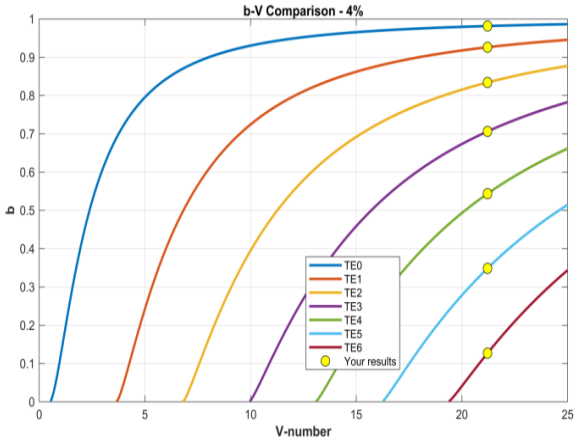

Figure 17. Transverse electric (TE) mode b-V diagram directed by a linear exponential graded index of 4 wt% TeO_2 nanoparticles (NPs)

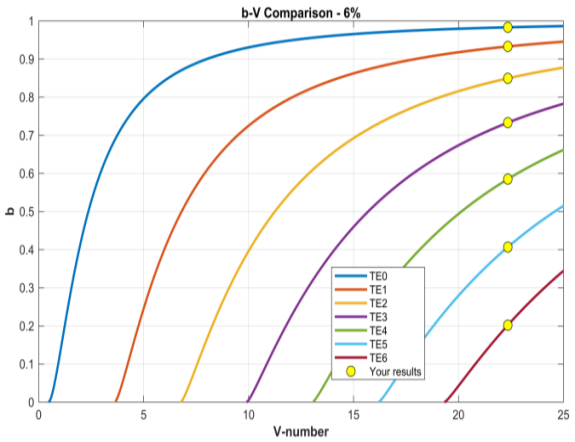

Figure 18. Transverse electric (TE) mode b-V diagram directed by a linear exponential graded index of 6 wt% TeO_2 nanoparticles (NPs)

Figures 15-18 show the b-V curves for various concentrations of TeO_2 (0%, 2%, 4%, and 6%) show normal dispersion characteristics of a slab waveguide, where a sharp increase in the normalized propagation parameter b is observed for lower values of normalized frequency V, followed by a gradual saturation for higher values of V, showing strong optical confinement for smaller thicknesses and stability for larger thicknesses of the waveguide; with an increase in concentration of TeO_2 from 0% to 6%, there is an increase in normalized frequency V from 7.66 to 22.34, resulting in a shift of dispersion curves to higher values due to an increase in refractive index, thereby improving the guiding capabilities of the waveguide, and an increase in the number of guided modes with an increase in concentration, where the sample with 0% concentration shows fewer guided modes compared to other concentrations (2%, 4%, and 6%); in addition, for all concentrations, the fundamental mode (TE_0) shows a higher *b*-value, indicating strong optical confinement in the core region, while other modes show lower *b*-values, indicating weaker optical confinement and higher penetration of the field in other regions; in addition, all *b*-value calculations fall in the range $0 < b < 1$, showing that all modes are guided, and *b*-value approaching 1 for fundamental modes in higher concentrations shows strong optical confinement, while lower *b*-value for other modes shows proximity to cut-off, which is in accordance with the theoretical dispersion characteristics of a slab waveguide [72, 73].

4.5 Analysis of transverse electric modes

Figure 19 depicts the electric field characteristic for a guided mode in a slab waveguide, which usually has an oscillating characteristic within the core region and an exponentially decaying characteristic outside the core region. This is in line with the waveguide's analytical solutions for the electric field [74].

Furthermore, the electric field characteristics for a slab waveguide are clearly shown in the above image; the electric field is more confined within the core region as the concentration of the nanoparticle is increased. This is demonstrated for the fundamental mode (TE_0), where the spatial breadth of the electric field is lower, and the electric field profile is compressed. Furthermore, the electric field outside the core region has compressed evanescent tails, suggesting a faster decline. This is consistent with the observation that, as the refractive index increases, a greater percentage of the electric field is confined within the core region, as shown in Figure 19. A previous study [68] discusses this phenomenon, showing that as the guiding layer parameters are increased, the electric field becomes more contained within the core region.

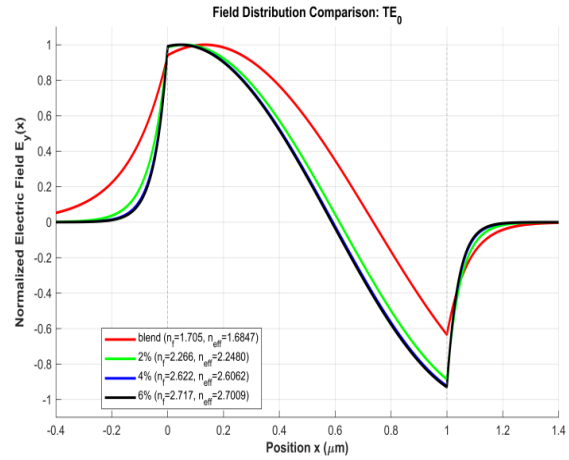

Figure 19. Transverse electric modes (TE_0) normalised electric field distributions (0, 2, 4, and 6 wt%) TeO_2 nanoparticles (NPs)

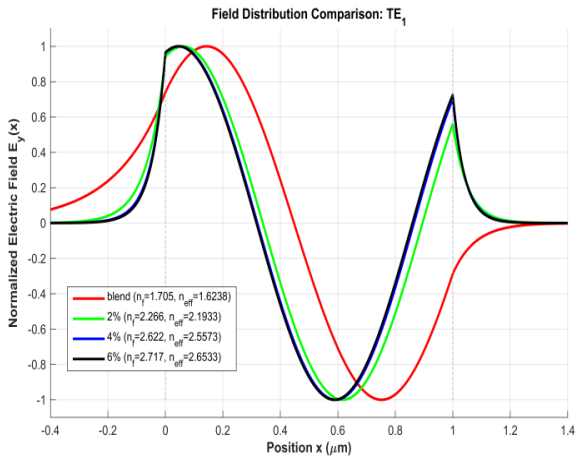

Figure 20. Transverse electric modes (TE_1) normalised electric field distributions (0, 2, 4, and 6 wt%) TeO_2 nanoparticles (NPs)

The higher-order modes (TE_2 and TE_2) in Figures 20 and 21 also show how the electric field lobes compress as the nanoparticle concentration increases. As the refractive index increases, the electric field is compressed and more localised within the core region, although the electric field for the higher-order modes naturally has one and two nodes for the TE_1 and TE_2 modes, respectively. This example demonstrates how a waveguide's mode number and electric-field properties are related and discusses this phenomenon [75, 76].

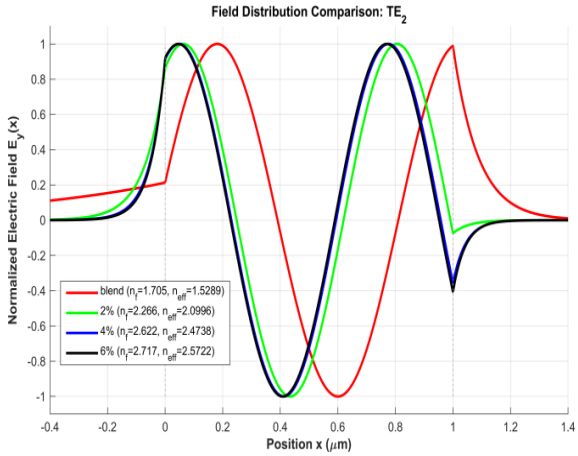

Figure 21. Transverse electric modes (TE_2) normalised electric field distributions (0, 2, 4, 6 wt%) TeO_2 nanoparticles (NPs)

4.6 Calculation of absorption loss (α_{abs})

One effect that results from absorption losses in the optical waveguides is that of reducing the guided waves because of the absorption characteristics of the waveguide material, where the optical waves are transformed into internal energy, leading to an exponential decrease in the intensity of light with propagation distance, expressed as $I(z) = I_0 e^{-\alpha z}$. Loss arising from absorption was calculated based on the absorption coefficient at a wavelength of 633 nm. Loss was then converted to decibel attenuation per unit length using:

$$\text{Loss}_{abs}\,(\text{dB/cm}) = 4.343\ \alpha\ (\text{cm}^{-1}) \qquad (21)$$

Table 9. Calculation of absorption loss (α_{abs})

TeO_2 (wt%)	α (cm^{-1})	Loss_{abs} (dB/cm)
0	0.0679276	0.2950
2	0.1503526	0.6531
4	0.2006048	0.8714
6	0.2230067	0.9685

As presented in Table 9, it is observed that an increase in concentration of TeO_2 leads to a corresponding increase in the waveguide's absorption loss. Specifically, the loss increases from approximately 0.295 dB/cm to a maximum value of 0.968 dB/cm for the 6 wt% doped sample. This may have been a result of the incorporation of the nanoparticles, which could improve the absorption of the light waves in the visible region by the increase in electronic absorption or creation of extra absorption centers within the polymer or internal scattering. It should be observed that the values for 4% and 6% doping are numerically quite similar, which may imply that there is a tendency to saturate the absorption within the specified wavelength region. It should also be observed that the values indicated above are solely for the absorption based on the absorption coefficient, whereas the total attenuation in the guide may have additional components [77].

5. PRACTICAL OPTIMIZATION THROUGH MATERIAL TRADE-OFF ANALYSIS

In order to assess the practical applicability and resource efficacy of the developed PMMA-PS/TeO_2 optofluidic photonic films, an analysis that involves a balance between the optical performance of the materials, process difficulty and material inputs was conducted. Increasing the weight percent of the nanoparticle material TeO_2 provides a useful improvement in terms of the refractive index (n) "per wt%," which results in an increased efficiency in the confinement and propagation of the TE waveguide modes in the asymmetric slab waveguide. On the other hand, the increase in the optical transmittance would be at the expense of the enhanced effects of Rayleigh scattering and localized absorption due to the nanoparticle presence, especially in the ultraviolet region. In terms of process difficulty, beyond 4 wt% of nanoparticle materials, there would be agglomeration within the chloroform medium, hence increasing the required time for ultrasonication and causing defects during manual casting. Since tellurium dioxide is much more expensive compared to bulk PMMA and PS, minimizing the weight percent of the former in terms of the economic factor would be preferable. Thus, the optimal loading weight percent would be around 4 wt%, which provides both refractive index contrast and transparency.

6. CONCLUSIONS

In this work, PMMA-PS/TeO_2 NCs were prepared, and their linear, nonlinear, and wave guiding characteristics were investigated. The experimental data showed that the concentration of TeO_2 NPs has a significant effect on the linear characteristics of the PMMA-PS/TeO_2 NCs, as shown by the increase in absorbance, decrease in optical bandgap, and increase in refractive index. The nonlinear characteristics of the PMMA-PS/TeO_2 NCs, as shown by the Z-scan data, revealed that the PMMA-PS/TeO_2 NCs possess a negative nonlinear refractive index along with a positive nonlinear absorption, which corresponds to a negative refractive index. Moreover, the nonlinear properties were highly sensitive to the concentration of TeO_2 NPs in the NCs. In addition, the results of the waveguide mode analysis reveal that the increase in the refractive index of the core layer enhances the refractive index difference, thereby increasing the normalized frequency and the number of guided modes. The guided mode indices are in agreement with the waveguide equation, and the electric field distribution for the TE mode in the waveguide reveals higher intensities in the core layer and a lower evanescent field in the surrounding media with increased TeO_2 NPs concentration. Thus, the PMMA-PS/TeO_2 NCs were found to possess linear, nonlinear, and waveguiding properties, making them useful for a variety of applications, including integrated optics, optical switching, and waveguide devices.

REFERENCES

[1] Jeeju, P.P., Jayalekshmi, S., Chandrasekharan, K.,

Sudheesh, P. (2013). Enhanced linear and nonlinear optical properties of thermally stable ZnO/poly(styrene)–poly(methyl methacrylate) nanocomposite films. Thin Solid Films, 531: 378-384. https://doi.org/10.1016/j.tsf.2012.12.043

[2] Anandalli, M.H., Bhajantri, R.F., Maidur, S.R., Patil, P.S. (2020). Fluorescence and third-order nonlinear optical properties of thermally stable CBPEA dye-doped PMMA/ZnO nanocomposites. Journal of Materials Science: Materials in Electronics, 31: 10531-10547. https://doi.org/10.1007/s10854-020-03601-6

[3] Kumar, A., Holuszko, M., Espinosa, D.C.R. (2017). E-waste: An overview on generation, collection, legislation and recycling practices. Resources, Conservation and Recycling, 122: 32-42. https://doi.org/10.1016/j.resconrec.2017.01.018

[4] Bouachrine, M., Ayachi, S. (2025). Organic electronics: Pioneering the future of sustainable and flexible technology. RSC Advances, 15(53): 45177-45195. https://doi.org/10.1039/d5ra04656d

[5] Butt, M.A. (2026). Flexible photonic waveguides and textiles: Materials, fabrication techniques, and emerging applications in wearable sensing. Materials Today Physics, 64: 102122. https://doi.org/10.1016/j.mtphys.2026.102122

[6] Mitaľová, Z., Kaščak, J., Kočiško, M., Litecká, J. (2026). Recycled thermoplastics for 3D printing filament production: A review of circular economy drivers, material behavior, and current research gaps. Polymers, 18(10): 1174. https://doi.org/10.3390/polym18101174

[7] Jagadeesh, P., Rangappa, S.M., Siengchin, S., et al. (2022). Sustainable recycling technologies for thermoplastic polymers and their composites: A review of the state of the art. Polymer Composites, 43(9): 5831-5862. https://doi.org/10.1002/pc.27000

[8] Mathur, V., Sharma, K. (2016). Thermal response of polystyrene/poly methyl methacrylate (PS/PMMA) polymeric blends. Heat and Mass Transfer, 52: 2901-2911. https://doi.org/10.1007/s00231-016-1779-4

[9] Saeed, A., Alzahrani, E., Morsi, M.A., et al. (2024). Enhanced optical and electrical properties of PEO/PMMA/TiO2 nanocomposites for optoelectronic applications. Optical Materials, 157: 116402. https://doi.org/10.1016/j.optmat.2024.116402

[10] Hussan, R.M., Mahdi, Z.F., Faris, R.A. (2019). Nonlinear optical properties of PMMA composites using Z-scan technique. Iraqi Journal of Laser, 12(Part A): 27-35. https://doi.org/10.31900/ijl.v12iA.82

[11] Zafar, M.S. (2020). Prosthodontic applications of polymethyl methacrylate (PMMA): An update. Polymers, 12(10): 2299. https://doi.org/10.3390/polym12102299

[12] Yabagi, J.A., Kimpa, M.I., Muhammad, M.N., Rashid, S.B., Zaidi, E., Agam, M.A. (2018). The effect of gamma irradiation on chemical, morphology and optical properties of polystyrene nanosphere at various exposure time. IOP Conference Series: Materials Science and Engineering, 298(1): 012004. https://doi.org/10.1088/1757-899X/298/1/012004

[13] Alwan, T.J. (2012). Gamma irradiation effect on the optical properties and refractive index dispersion of dye doped polystyrene films. Turkish Journal of Physics, 36(3): 377-384. https://doi.org/10.3906/fiz-1107-5

[14] Ding, Y., Abeykoon, C., Perera, Y.S. (2022). The effects of extrusion parameters and blend composition on the mechanical, rheological and thermal properties of LDPE/PS/PMMA ternary polymer blends. Advanced Industrial and Manufacturing Engineering, 4: 100067. https://doi.org/10.1016/j.aime.2021.100067

[15] Rostami, A., Nazockdast, H., Karimi, M., Javidi, Z. (2016). Role of multiwalled carbon nanotubes localization on morphology development of PMMA/PS/PP ternary blends. Advances in Polymer Technology, 35(1): 21530. https://doi.org/10.1002/adv.21530

[16] Nouh S.A., Benthami K.A., AlSomali F., Yajzey R., Bakeer D.E.S. (2024). Impact of gamma radiation on the linear and nonlinear optical properties of PVA/CMC/ZnS-NiO nanocomposite films. Radiation Effects and Defects in Solids, 179(1-2): 43-63. https://doi.org/10.1080/10420150.2024.2318710

[17] Shanshool, H.M. (2016). Linear and nonlinear optical properties of polymer-ZnO-CuO nanocomposites. Ph.D. thesis. Universiti Kebangsaan Malaysia, Bangi, Malaysia. https://ptsldigital.ukm.my/jspui/handle/123456789/499810.

[18] Hrabovsky, J., Strizik, L., Desevedavy, F., et al. (2024). Optical, magneto-optical properties and fiber-drawing ability of tellurite glasses in the TeO2–ZnO–BaO ternary system. Journal of Non-Crystalline Solids, 624: 122712. https://doi.org/10.1016/j.jnoncrysol.2023.122712

[19] Tan, W.J., Wang, X.F., Wei, R.Q., et al. (2024). Ag2[TeO2(OH)4]: A nonlinear optical tellurate with balanced comprehensive performance. Journal of Materials Chemistry C, 12(34): 13632-13638. https://doi.org/10.1039/d4tc02218a

[20] Maidur, S.R., Patil, P.S. (2019). Linear optical and third-order nonlinear optical properties of anthracene chalcone derivatives doped PMMA thin films. Optik, 190: 54-67. https://doi.org/10.1016/j.ijleo.2019.05.092

[21] Van Stryland, E.W., Sheik-Bahae M. (1997). Z-scan technique for nonlinear materials characterization. Materials Characterization and Optical Probe Techniques: A Critical Review, 10291: 488-511. https://doi.org/10.1117/12.279853

[22] Almusawe, A.J., Rahma, M.A., Mohammed, E.A., Saadon, H.L. (2020). Application of Z-scan technique for the study of nonlinear optical properties of BCP/MEHPPV. Nonlinear Optics, Quantum Optics, 1-11. https://faculty.uobasrah.edu.iq/uploads/publications/1584726498.pdf.

[23] Artkın, F. (2022). Z-scan technique and engineering applications for nonlinear optical measurements. In New Trends in Engineering Sciences, pp. 181-190.

[24] Orfanos, I., Aloukos, P., Kaloudi-Chantzea, A., Pistolis, G., Couris, S. (2025). Efficient tuning of the third-order nonlinear optical properties of some functionalized boron-dipyrromethene dyes. Nanomaterials, 15(20): 1549. https://doi.org/10.3390/nano15201549

[25] Chen, S., Niu, R., Gao, Y., et al. (2024). Tunable nonlinear absorption of gold nanostars and application as a saturable absorber. Optics & Laser Technology, 168: 109873. https://doi.org/10.1016/j.optlastec.2023.109873

[26] Mahdi, M.A., Hasan, Z.A., Al-Ammar, K. (2026). Characterization and antibacterial activity of TeO2-reinforced PMMA–PS nanocomposites developed by

solution casting method. Iraqi Journal of Applied Physics, 22(2): 281-288. https://ijap-iq.com/index.php/ijap/article/view/490/206.
[27] Ahmed, G., Hashim, A. (2023). Synthesis of PMMA/PEG/Si3N4 nanostructures and exploring the structural and dielectric characteristics for flexible nanoelectronics applications. Silicon, 15: 3977-3985. https://doi.org/10.1007/s12633-023-02322-9
[28] Hashim, A., Hadi, Q. (2017). Novel of (niobium carbide/polymer blend) nanocomposites: Fabrication and characterization for pressure sensors. Sensor Letters, 15: 951-953. https://doi.org/10.1166/sl.2017.3892
[29] Kadhim, M.A., Al-Bermany, E. (2021). New fabricated PMMA-PVA/graphene oxide nanocomposites: Structure, optical properties and application. Journal of Composite Materials, 55(20): 2793-2806. https://doi.org/10.1177/0021998321995912
[30] Rashid, F.L., Hashim, A., Habeeb, M.A., Salman, S.R., Ahmed, H. (2013). Preparation of (PS-PMMA) copolymer and study the effect of sodium fluoride on its optical properties. Chemistry and Materials Research, 3(7): 55-58.
[31] Habeeb, M.A., Hashim, A., Hadi, A. (2017). Fabrication of new nanocomposites: CMC-PAA-PbO2 nanoparticles for piezoelectric sensors and gamma radiation shielding applications. Sensor Letters, 15: 785-790. https://doi.org/10.1166/sl.2017.3877
[32] Hameed, N.J., Haider, A.J., Hawy, R.E. (2019). Optical properties study for PS/PMMA blend as laser active medium. AIP Conference Proceedings, 2123(1): 020022. https://doi.org/10.1063/1.5116949
[33] Acharya, A.D., Sarwan, B., Malik, I.A., Bhat, Y.A., Silwal, K., Rathore, M.K. (2019). Optical properties of NiO:PVA thin films. AIP Conference Proceedings, 2100(1): 020006. https://doi.org/10.1063/1.5098560
[34] Allen, P.B. (1975). Solid State Physics by H. E. Hall. American Journal of Physics, 43: 929-933. https://doi.org/10.1119/1.9981
[35] Viezbicke, B.D., Patel, S., Davis, B.E., Birnie, D.P. (2015). Evaluation of the Tauc method for optical absorption edge determination: ZnO thin films as a model system. Basic Solid State Physics, 252(8): 1700-1710. https://doi.org/10.1002/pssb.201552007
[36] Shanshool, H.M., Yahaya, M., Yunus, W.M.M., Abdullah, I.Y. (2016). Investigation of energy band gap in polymer/ZnO nanocomposites. Journal of Materials Science: Materials in Electronics, 27: 9804-9811. https://doi.org/10.1007/s10854-016-5046-8
[37] Mohaisen, A., Hamad, Z. (2019). Fabrication and characterization of polymer blend doped with metal carbide nanoparticles for humidity sensors. Journal of Nanostructures, 9(2): 340-348. https://doi.org/10.22052/JNS.2019.02.016
[38] Tański, T., Matysiak, W., Krzemiński, Ł. (2017). Analysis of optical properties of TiO2 nanoparticles and PAN/TiO2 composite nanofibers. Materials and Manufacturing Processes, 32(11): 1218-1224. https://doi.org/10.1080/10426914.2016.1257129
[39] Matamoros-Ambrocio, M., Sánchez-Mora, E., Gómez-Barojas, E., Luna-López, J.A. (2021). Synthesis and study of the optical properties of PMMA microspheres and opals. Polymers, 13(13): 2171. https://doi.org/10.3390/polym13132171
[40] Hussien, H.A.J., Hashim, A. (2024). Fabrication and analysis of PVA/TiC/SiC hybrid nanostructures for nanoelectronics and optics applications. Journal of Inorganic and Organometallic Polymers and Materials, 34: 2716-2727. https://doi.org/10.1007/s10904-024-03007-5
[41] Hashim, A., Habeeb, M.A., Khalaf, A., Hadi, A. (2017). Fabrication of (PVA-PAA) blend-extracts of plants bio-composites and studying their structural, electrical and optical properties for humidity sensors applications. Sensor Letters, 15(7): 589-596. https://doi.org/10.1166/sl.2017.3856
[42] Sabbah, S., Hasan, M., Yehiaa, B., Satar, Z. (2016). The effect of metal powder on the optical properties of polyvinyl acetate. Journal of Advanced Research in Applied Sciences, 3(1): 1-6. https://doi.org/10.53555/nnas.v3i1.666
[43] Zhang, X., Wei, S.Y., Haldolaarachchige, N., et al. (2012). Magnetoresistive conductive polyaniline–barium titanate nanocomposites with negative permittivity. The Journal of Physical Chemistry C, 116(29): 15731-15740. https://doi.org/10.1021/jp303226u
[44] Singh, C.H., Devi, K.N., Sarma, H.N.K. (2011). Optical and structural properties of thermally evaporated CdS thin films. AIP Conference Proceedings, 1372(1): 313-317. https://doi.org/10.1063/1.3644462
[45] Hashim, A., Jassim, A. (2018). Novel of biodegradable polymers-inorganic nanoparticles: Structural, optical and electrical properties as humidity sensors and gamma radiation shielding for biological applications. Journal of Bionanoscience, 12(2): 170-176. https://doi.org/10.1166/jbns.2018.1518
[46] Mustafa, F.A. (2013). Optical properties of NaI doped polyvinyl alcohol films. Physical Science Research International, 1(1): 1-9. https://www.netjournals.org/pdf/PSRI/2013/1/12-011.pdf.
[47] Alshammari, A.H., Alshammari, M., Alshammari, K., Allam, N.K., Taha, T.A. (2023). PVC/PVP/SrTiO3 polymer blend nanocomposites as potential materials for optoelectronic applications. Results in Physics, 44: 106173. https://doi.org/10.1016/j.rinp.2022.106173
[48] Jaafar, H.K., Hashim, A., Rabee, B.H. (2023). Fabrication and tuning the morphological and optical characteristics of PMMA/PEO/SiC/BaTiO3 newly quaternary nanostructures for optical and quantum electronics fields. Optical and Quantum Electronics, 55: 989. https://doi.org/10.1007/s11082-023-05208-7
[49] Ahmed, H., Abduljalil, H.M., Hashim, A. (2019). Novel studies on spectroscopic, optical and electronic properties of (PVA-TiO2/SiC) nanocomposites for biological and optoelectronics applications. Advanced Science, Engineering and Medicine, 11(6): 554-564. https://doi.org/10.1166/asem.2019.2389
[50] Abdullah, O.G., Aziz, S.B., Ome,r K.M., Salih, Y.M. (2015). Reducing the optical band gap of polyvinyl alcohol (PVA) based nanocomposite. Journal of Materials Science: Materials in Electronics, 26: 5303-5309. https://doi.org/10.1007/s10854-015-3067-3
[51] Rajesh, K., Crasta, V., Rithin Kumar, N.B., Shetty, G., Rekha, P.D. (2019). Structural, optical, mechanical and dielectric properties of titanium dioxide doped PVA/PVP nanocomposite. Journal of Polymer Research, 26: 99. https://doi.org/10.1007/s10965-019-1762-0

[52] Abdullah, O.G., Salman, Y.A.K., Saleem, S.A. (2015). In-situ synthesis of PVA/HgS nanocomposite films and tuning optical properties. Physical Materials and Chemistry, 3(2): 18-24. http://pubs.sciepub.com/pmc/3/2/1.

[53] Liu, S.P., Islam, M.D., Ku, Z., et al. (2021). Novel computational design of high refractive index nanocomposites and effective refractive index tuning based on nanoparticle morphology effect. Composites Part B: Engineering, 223: 109128. https://doi.org/10.1016/j.compositesb.2021.109128

[54] Habeeb, M.A., Oreibi, I., Hamza, R.S.A., Mamoun, F. (2025). Synthesis and tuning the morphological, structural, optical and dielectric features of SiO2/CuO futuristic nanocomposites doped PVA–PEG for optoelectronic and energy storage applications. Journal of Inorganic and Organometallic Polymers and Materials, 35: 2391-2405. https://doi.org/10.1007/s10904-024-03334-7

[55] James, J. (2019). Refractive index engineering using polymer nanocomposites. Ph.D. dissertation. Université de Bretagne Sud. https://theses.hal.science/tel-03086200v1/file/2019theseJemyJ.pdf.

[56] Aziz, S.B., Brza, M.A., Nofal, M.M., et al. (2020). A comprehensive review on optical properties of polymer electrolytes and composites. Materials, 13(17): 3675. https://doi.org/10.3390/ma13173675

[57] Srikanth, C., Sridhar, B.C., Prasad, M.V.N., Mathad, R.D. (2016). Characterization and DC conductivity of novel ZnO doped polyvinyl alcohol (PVA) nano-composite films. Journal of Advanced Physics, 5(2): 105-109. https://doi.org/10.1166/jap.2016.1235

[58] Al-Ahmad, A.Y., Al-Mudhaffer, M.F., Badran, H.A., Emshary, C.A. (2013). Nonlinear optical and thermal properties of BCP: PMMA films determined by thermal self-diffraction. Optics & Laser Technology, 54: 72-78. https://doi.org/10.1016/j.optlastec.2013.05.009

[59] Sheik-Bahae, M., Said, A.A., Wei, T.H., Hagan, D.J., Van Stryland, E.W. (1990). Sensitive measurement of optical nonlinearities using a single beam. IEEE Journal of Quantum Electronics, 26(4): 760-769. https://doi.org/10.1109/3.53394

[60] Sheik-Bahae, M., Van Stryland, E. (1998). Z-scan measurements of optical nonlinearities. In Characterization Techniques and Tabulations for Organic Nonlinear Optical Materials, pp. 655-692.

[61] Dorranian, D., Golian, Y., Hojabri, A. (2023). Investigation of nitrogen plasma effect on the nonlinear optical properties of PMMA. Journal of Theoretical and Applied Physics, 6(1): 1-8. https://doi.org/10.1186/2251-7235-6-1

[62] Praveen, P.A., Babu, R.R., Jothivenkatachalam, K., Ramamurthi, K. (2015). Spectral, morphological, linear and nonlinear optical properties of nanostructured benzimidazole metal complex thin films. Spectrochimica Acta Part A: Molecular and Biomolecular Spectroscopy, 150: 280-289. https://doi.org/10.1016/j.saa.2015.05.074

[63] Haripadmam, P.C., Kavitha, M.K., John, H., Krishnan, B., Gopinath, P. (2012). Optical limiting studies of ZnO nanotops and its polymer nanocomposite films. Applied Physics Letters, 101: 071103. https://doi.org/10.1063/1.4745605

[64] Sreeja, R., John, J., Aneesh, P.M., Jayaraj, M.K. (2010). Linear and nonlinear optical properties of luminescent ZnO nanoparticles embedded in PMMA matrix. Optics Communications, 283(14): 2908-2913. https://doi.org/10.1016/j.optcom.2010.02.044

[65] Rubin, M. (1985). Optical properties of soda lime silica glasses. Solar Energy Materials, 12(4): 275-288. https://doi.org/10.1016/0165-1633(85)90052-8

[66] Kogelnik, H., Ramaswamy, V. (1974). Scaling rules for thin-film optical waveguides. Applied Optics, 13(8): 1857-1862. https://doi.org/10.1364/AO.13.001857

[67] Chen, C.L. (2005). Foundations for Guided-Wave Optics. John Wiley & Sons. https://doi.org/10.1002/0470042222

[68] Taya, S.A., Elwasife, K.Y. (2014). Field profile of asymmetric slab waveguide structure with LHM layers. Journal of Nano- and Electronic Physics, 6(2): 02007. https://jnep.sumdu.edu.ua/en/full_article/1237.

[69] Bhattacharyya, S., Thander, A.K. (2024). Slab waveguide communication study using Finite Difference Method (FDM) with fourth-order compact scheme. Results in Optics, 16: 100681. https://doi.org/10.1016/j.rio.2024.100681

[70] Buus, J. (1980). Dispersion of TE modes in slab waveguides with reference to double heterostructure semiconductor lasers. Applied Optics, 19(12): 1987-1989. https://doi.org/10.1364/AO.19.001987

[71] Mamanou, A., Khelfaoui, F., Aiadi, K.E. (2014). Calculation of effective index for different dielectric waveguides structures made of PVCi/PMATRIFE polymers at telecom-wavelength λ=1.55 μm. Optical and Quantum Electronics, 46: 235-245. https://doi.org/10.1007/s11082-013-9772-3

[72] Hussein, A.J., Nassar, Z.M., Taya, S.A. (2021). Dispersion properties of slab waveguides with a linear graded-index film and a nonlinear substrate. Microsystem Technologies, 27: 2589-2594. https://doi.org/10.1007/s00542-020-05016-z

[73] Hussein A.J., Taya, S.A., Vigneswaran, D., et al. (2021). Universal dispersion curves of a planar waveguide with an exponential graded-index guiding layer and a nonlinear cladding. Results in Physics, 20: 103734. https://doi.org/10.1016/j.rinp.2020.103734

[74] Ramza, H., Nasimi, F., Ishak, K.A., Ab-Rahman, M.S. (2012). Analysis of TE (Transverse Electric) modes of symmetric slab waveguide. Advanced Studies in Theoretical Physics, 6(27): 1323-1336. https://www.m-hikari.com/astp/astp2012/astp25-28-2012/ramzaASTP25-28-2012.pdf.

[75] Marcuse, D. (2013). Theory of Dielectric Optical Waveguides. Elsevier.

[76] Kogelnik, H. (1988). Theory of optical waveguides. In Guided-Wave Optoelectronics, pp. 7-88. https://doi.org/10.1007/978-3-642-97074-0_2

[77] Pitois, C., Hult, A., Wiesmann, D. (2001). Absorption and scattering in low-loss polymer optical waveguides. Journal of the Optical Society of America B, 18(7): 908-912. https://doi.org/10.1364/JOSAB.18.000908